American Mineralogist, Volume 103, pages 1988–1998, 2018

Raman modes of carbonate minerals as pressure and temperature gauges up to 6 GPa and 500 °C

Stefan Farsang[1,*], Sébastien Facq[1], and Simon A.T. Redfern[1,2]

[1]Department of Earth Sciences, University of Cambridge, Downing Street, Cambridge, CB2 3EQ, U.K.
[2]Center for High Pressure Science and Technology Advanced Research (HPSTAR), Shanghai 201203, China

Abstract

Diamond-anvil cell (DAC) experiments focusing on the solubility of carbonates and aqueous carbon speciation at subduction zones require pressure monitoring with sensitive, chemically inert sensors. Commonly used pressure indicators are either too insensitive or prone to contaminate pressure-transmitting media due to their increased solubility at high pressure and/or temperature (*P-T*). Here, the *P*- and *T*-induced frequency shifts of the Raman vibrational modes of natural crystalline carbonate minerals aragonite, calcite, dolomite, magnesite, rhodochrosite, and siderite have been calibrated for application as Raman spectroscopic *P* and *T* sensors in DACs up to 500 °C and 6 GPa. The shifts of all modes are quasi-constant over the observed *P* and *T* ranges and are generally less prominent for internal modes than for external modes. Our method provides a sensitive and robust alternative to traditional pressure calibrants, and has three principal advantages: (1) higher sensitivity (for particular Raman vibrational modes), (2) monitoring *P-T*-induced shifts of several modes allows even more accurate *P-T* determination, and (3) no contamination of pressure-transmitting media by foreign materials can occur. Additionally, the isobaric and isothermal equivalent of the Grüneisen parameter and the anharmonic parameter for each of the traced modes have been determined.

Keywords: Aragonite, calcite, diamond-anvil cell, dolomite, high pressure, high temperature, magnesite, pressure sensor, Raman spectroscopy, rhodochrosite, siderite, temperature sensor

Introduction

Carbonate minerals are the dominant carbon-bearing phases within Earth's crust and lithospheric mantle, representing the most stable carbon-bearing phases down to depths of at least 200 km, corresponding to pressures of up to ~6 GPa (e.g., Redfern 2000; Dasgupta et al. 2004; Dasgupta and Hirschmann 2006, 2010; Rohrbach and Schmidt 2011; Oganov et al. 2013). They are the primary carriers of carbon into the deeper Earth at subduction zones, and their behavior in the high *P-T* environments of the lithosphere determines how much, and on what timescales, carbon gets recycled to the atmosphere and hence oceans, or is retained in the mantle (e.g., Ague and Nicolescu 2014; Manning 2014; Kelemen and Manning 2015). Because of the important role carbonate minerals play in the key geological processes (such as subduction, arc volcanism, and dissolution in aqueous fluids) of the Earth's deep carbon cycle, the accurate determination of their physical and chemical properties under high *P* and *T* conditions is of great importance. The interest in the topic is reflected by a significant and increasing number of experimental studies based on the coupling of Raman spectroscopy with DAC techniques to understand the properties of carbonate minerals at conditions corresponding to planetary interiors (Liu and Mernagh 1990; Kraft et al. 1991; Williams et al. 1992; Gillet et al. 1993; Lin and Liu 1997; Minch et al. 2010a, 2010b, Farfan et al. 2012, 2013; Spivak et al. 2014; Facq et al. 2014, 2016; Cerantola et al. 2015; Chaney et al. 2015; Pippinger et al. 2015; Xu et al. 2015; Liu et al. 2016; Müller et al. 2016; Koch-Müller et al. 2016; Maruyama et al. 2017; Chariton et al. 2017).

Monitoring, recording, and reproducing extensive thermodynamic variables such as pressure and temperature is crucial for any high *P-T* study and is a particular requirement in diamond-anvil cell (DAC) experiments. Pressure is typically measured in such experiments based on the Raman or fluorescence frequency shifts of a calibrant inside the compression chamber (e.g., ruby or diamond). The principal limitations of traditionally used optical pressure sensors of this type are discussed here. Ruby, a Cr^{3+}-doped α-Al_2O_3, is the most extensively used pressure sensor (Barnett et al. 1973; Datchi et al. 2007). Broadening of the ruby R_1 and R_2 fluorescence peaks and the decreasing signal-to-background ratio at high temperatures and the large uncertainty on the pressure and temperature cross derivative of the frequency, all significantly reduce the accuracy of pressure determination (Ragan et al. 1992; Goncharov et al. 2005; Datchi et al. 2007). A further complication is the chemical dissolution of ruby into water (the pressure medium), due to its increased solubility at high *P-T* conditions (Tropper and Manning 2007; Andreani et al. 2013). This may become particularly significant in DAC experiments that aim to determine the solubility of carbonates and aqueous carbon speciation via carbonate–water equilibria since these experiments assume no chemical interaction between the pressure-transmitting medium and the pressure sensor. For this reason, it is imperative that the use of pressure sensors made of materials soluble in the fluid phase in the DAC at high *P-T* is

* E-mail: sf571@cam.ac.uk

0003-004X/18/0012–1988$05.00/DOI: https://doi.org/10.2138/am-2018-6442

Downloaded from https://pubs.geoscienceworld.org/msa/ammin/article-pdf/103/12/1988/4574485/am-2018-6442.pdf
by University of Arizona user
on 17 December 2018

avoided. Other pressure sensors, including $SrB_4O_7:Sm^{2+}$, quartz, α-SiO_2, and berlinite, $AlPO_4$, also exhibit increased solubility at high *T*, making them unusable in solubility and aqueous speciation experiments (Manning 1994; Datchi et al. 2000; Watenphul and Schmidt 2012). The use of zircon, $ZrSiO_4$, which is only soluble at the parts per million level in high *P-T* fluids (Bernini et al. 2013), should also be avoided, as even low concentrations of contaminants can affect the solubility of phases and corresponding aqueous speciation. Although stable over a large *P-T* range, and chemically inert, ^{12}C and ^{13}C diamond, and cubic boron nitride show relatively low pressure-sensitivity (2.83, 2.83, and 3.27 cm^{-1}/GPa, respectively), which has a deleterious effect on the precision of pressure determination (Schiferl et al. 1997; Grasset et al. 2005; Datchi et al. 2007). Furthermore, below 13 GPa the Raman signal from the ^{12}C diamond is hidden by the strong signal produced by the diamond anvils, while ^{13}C diamond, which could be used in this *P* range, is not readily available (Datchi et al. 2007).

Instead of introducing foreign material to the compression chamber to measure *P* and/or *T*, here we propose the use of frequency shifts of the Raman vibrational modes of the crystalline carbonates themselves (cross-calibrated against the ruby R_1 fluorescence peak) as *P-T* sensors. Indeed, most of the Raman vibrational modes of carbonates are particularly sensitive to subtle *P-T* changes. The simultaneous monitoring of the behavior of multiple modes of varying sensitivity provides an additional route for an even more accurate determination of *P-T* conditions. Moreover, by avoiding the introduction of foreign material into the DAC, the possibility of its interaction with aqueous media is ruled out. This alternative method has been recently employed in carbon aqueous speciation experiments of aqueous fluids in equilibrium with aragonite at subduction zone environmental conditions (Facq et al. 2014, 2016).

Here, we report *P*- and *T*-induced frequency shifts of the Raman vibrational modes of natural aragonite ($CaCO_3$), calcite ($CaCO_3$), dolomite [$CaMg(CO_3)_2$], magnesite ($MgCO_3$), rhodochrosite ($MnCO_3$), and siderite ($FeCO_3$) up to 6–6.5 GPa and 400–500 °C, respectively. From these data, the isobaric and isothermal equivalent of the Grüneisen parameter and the anharmonic parameter for the corresponding vibrational modes were calculated to provide a robust method for combined *P-T* measurement in the DAC.

Experimental methods

High-purity, naturally occurring carbonate minerals were used in all experiments, including aragonite from Landes, France; calcite from Miskolctapolca, Hungary; dolomite from Campolongo, Italy; magnesite from Hnúšťa, Slovakia; rhodochrosite from Colorado, U.S.A.; and siderite from Tincroft Mine, Cornwall, U.K. All carbonate minerals were characterized by X-ray diffraction (XRD), electron probe microanalysis, and Raman spectroscopy prior to investigation. The unit-cell parameters and measured chemical formulas are reported in Table 1.

The high-*P* experiments were conducted at room *T* in a membrane-type diamond-anvil cell (Letoullec et al. 1988) equipped with IIa diamond anvils with culet diameters of 500 μm. A pressure-transmitting medium and some natural carbonate single crystals were loaded in a pre-indented (initially 240 μm and after indentation 100 μm) thick steel gasket, drilled with a 200 μm diameter hole. The pressure-transmitting medium comprised a 4:1 methanol-ethanol fluid mixture, which is hydrostatic over the full pressure range of our experiments (Klotz et al. 2009). The pressure inside the compression chamber was increased from ~0 to ~6 GPa in pressure increments of ~0.5 GPa using a PDS 200 pneumatic drive system (BETSA). The pressure was calculated from the calibrated shift of the ruby R_1 fluorescence line (Mao et al. 1986) after at least 30 min of response time required for the ruby fluorescence peak to reach its equilibrium value (Picard et al. 2006).

The high-*T* experiments were conducted at room *P* using a DSC600 heating stage (Linkam Scientific Instruments) with the sample held within an aluminum sample pan. The temperature was gradually increased from 25 to 425 °C for rhodochrosite and siderite and to 500 °C for the other carbonates in temperature increments of 25 °C using a TMS94 temperature controller (Linkam Scientific Instruments).

Raman spectra were collected in the 100–1800 cm^{-1} spectral range using a confocal LabRAM 300 (Horiba Jobin Yvon) Raman spectrometer of 300 mm focal length. A holographic grating of 1800 gr/mm coupled to a Peltier front illuminated CCD detector (1024 × 256 pixel in size) enabled a spectral resolution of ~1 cm^{-1}. The excitation line at 532.05 nm was produced by a Ventus 532 laser source (Laser Quantum) focused on the sample using an Olympus LMPLFLN 50× long working distance objective.

All Raman spectra were treated by PeakFit software. For each Raman spectrum, the baseline was subtracted and peak features were determined by least-squares fitting to Voigt profiles for the Raman bands. Peak positions were calibrated against the measured excitation of a Ne light reference spectrum (Saloman and Sansonetti 2004).

Results and discussion

Raman-active modes

Aragonite crystallizes in space group *Pmcn*. Its orthorhombic cell contains 20 atoms per lattice point and its 57 vibrational modes can be classified as

$$\Gamma = 9A_g + 6A_u + 6B_{1g} + 8B_{1u} + 9B_{2g} + 5B_{2u} + 6B_{3g} + 8B_{3u}$$

of which the gerade A_g, B_{1g}, B_{2g}, and B_{3g} modes are Raman-active (De La Pierre et al. 2014). Of these 30, 20 modes were observed in the Raman spectrum taken at 25 °C (Fig. 1). The vibrational modes located in the low-frequency range at 115, 125, 145, 155, 164, 182, 192, 208, 216, 250, 263, 274, and 285 cm^{-1} represent external or lattice modes, resulting from the interactions between Ca^{2+} and CO_3^{2-} ions. The high-frequency vibrational modes ν_4 at 701, 705, and 716 cm^{-1}; ν_2 at 853 cm^{-1}; ν_1 at 1085 cm^{-1}; and ν_3 at 1463 and 1576 cm^{-1} represent internal modes of the CO_3^{2-} group (Gillet et al. 1993). Of these, 14 could be traced across the entire pressure range of investigation, and 11 could be traced up to temperatures of the aragonite-calcite phase transition.

Calcite, magnesite, rhodochrosite, and siderite all crystallize in space group $R\bar{3}c$. Their rhombohedral primitive cell contains

Table 1. Compositions and unit-cell parameters of carbonate minerals used

Sample	Ideal formula	Calculated formula	Space group	Unit-cell parameters (Å)		
				a	*b*	*c*
Aragonite	$CaCO_3$	$Ca_{1.00}CO_3$	*Pmcn*	4.9612(5)	7.9701(9)	5.7420(4)
Calcite	$CaCO_3$	$Ca_{1.00}CO_3$	$R\bar{3}c$	4.9864(2)		17.0491(8)
Dolomite	$CaMg(CO_3)_2$	$Ca_{0.50}Mg_{0.50}CO_3$	$R\bar{3}$	4.8069(4)		16.012(2)
Magnesite	$MgCO_3$	$Mg_{0.96}Ca_{0.01}Fe_{0.03}CO_3$	$R\bar{3}c$	4.6371(2)		15.0365(5)
Rhodochrosite	$MnCO_3$	$Mn_{0.99}Fe_{0.01}CO_3$	$R\bar{3}c$	4.7756(7)		15.669(2)
Siderite	$FeCO_3$	$Fe_{0.98}Mg_{0.01}Mn_{0.01}CO_3$	$R\bar{3}c$	4.6910(4)		15.379(2)

Downloaded from https://pubs.geoscienceworld.org/msa/ammin/article-pdf/103/12/1988/4574485/am-2018-6442.pdf
by University of Arizona user
on 17 December 2018

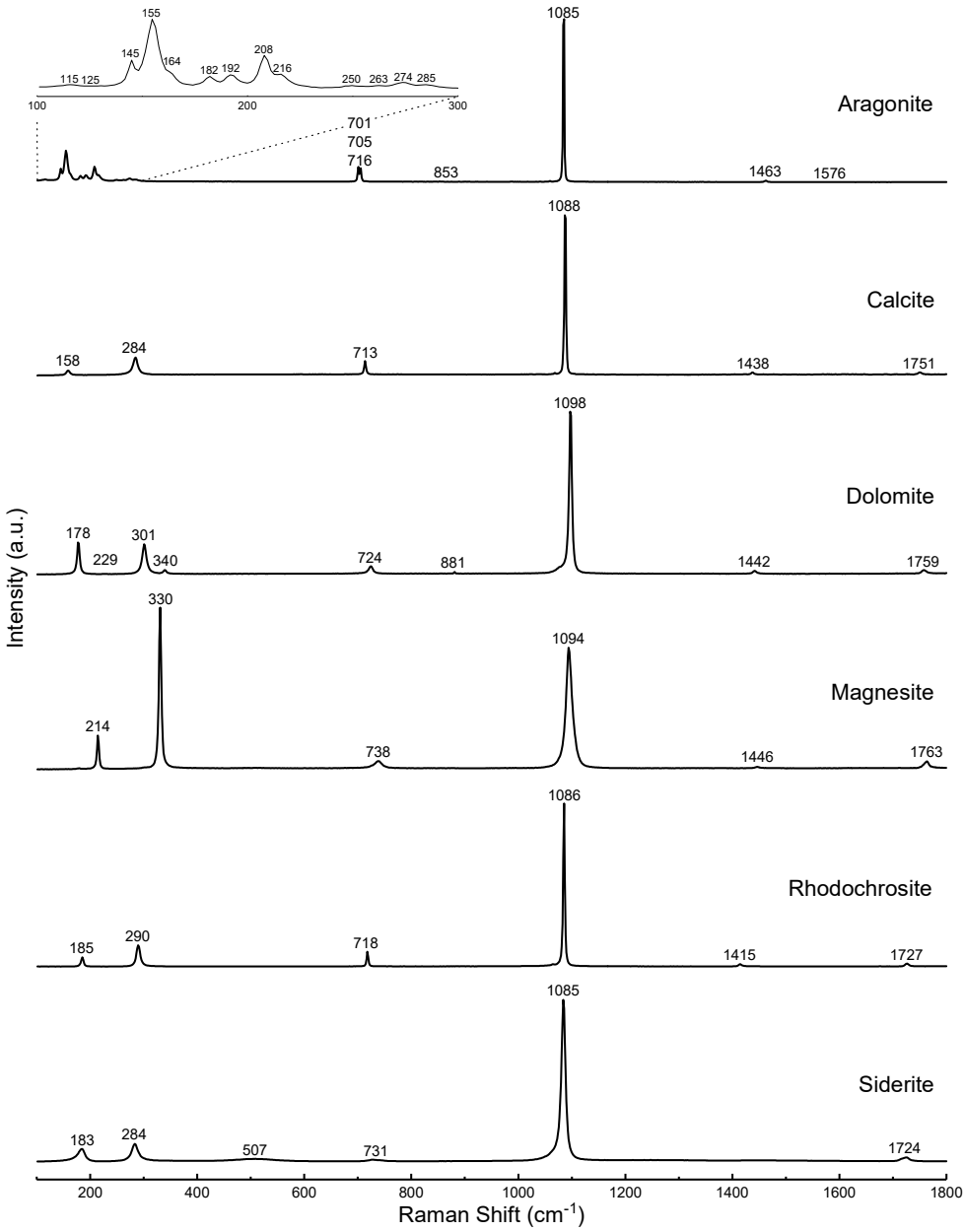

FIGURE 1. Raman spectra of carbonate minerals collected at ambient pressure (1 bar) and temperature (25 °C).

10 atoms per lattice point, and their 27 vibrational modes can be classified as

$$\Gamma = A_{1g} + 2A_{1u} + 3A_{2g} + 3A_{2u} + 4E_g + 5E_u$$

of which the gerade A_{1g} and E_g modes are Raman-active (Rutt and Nicola 1974; Valenzano et al. 2007; De La Pierre et al. 2014). All of these, apart from the ν_3 mode in siderite, were observed in the Raman spectrum taken at 25 °C (Fig. 1). The lack of the ν_3 mode in siderite is in agreement with Rutt and Nicola (1974). The low-frequency vibrational modes (158 and 284 cm^{-1} in calcite, and 330 cm^{-1} in magnesite, 185 and 290 cm^{-1} in rhodochrosite, and 183 and 284 cm^{-1} in siderite) represent external modes, resulting from the interactions between M^{2+} and CO_3^{2-} ions, M being Ca, Mg, Mn, and Fe, respectively. The high-frequency vibrational modes, ν_4 (713 cm^{-1} in calcite, 738 cm^{-1} in magnesite, 718 cm^{-1} in rhodochrosite, and 731 cm^{-1} in siderite), ν_1 (1088 cm^{-1} in calcite, 1094 cm^{-1} in magnesite, 1086 cm^{-1} in rhodochrosite, and 1085 cm^{-1} in siderite), and ν_3 (1438 cm^{-1} in calcite, 1446 cm^{-1} in magnesite, and 1415 cm^{-1} in rhodochrosite) represent internal modes of the CO_3^{2-} group. Silent mode ν_2 was absent and ν_3 (corresponding to the asymmetric CO_3 stretching with E_g symmetry) was not traced due to its highly asymmetric nature, which results from the existence of weak satellite excitations at the lower-frequency side of the main ν_3 Raman-active mode (Krishnamurti 1957). The high-

Downloaded from https://pubs.geoscienceworld.org/msa/ammin/article-pdf/103/12/1988/4574485/am-2018-6442.pdf
by University of Arizona user
on 17 December 2018

frequency mode at 1751 cm^{-1} in calcite, 1763 cm^{-1} in magnesite, 1727 cm^{-1} in rhodochrosite, and 1724 cm^{-1} in siderite represents the $2\nu_2$ overtone mode of the silent, IR-active ν_2 mode (Couture 1947). An additional broad, low-intensity feature at 507 cm^{-1} was observed and traced in siderite, which is caused by an Fe^{2+} electronic excitation (Popkov et al. 1972).

Dolomite crystallizes in space group $R\bar{3}$. It has 10 atoms per lattice point and its 27 vibrational modes can be classified as

$$\Gamma = 4E_g + 4A_g + 5E_u + 5A_u$$

of which the gerade A_g and E_g modes are Raman-active (Valenzano et al. 2007) and were observed in the Raman spectrum taken at 25 °C (Fig. 1). The modes at lower frequencies (178, 229, 301, and 340 cm^{-1}) represent external modes, resulting from the interactions between M^{2+} and CO_3^{2-} ions, M being both Ca and Mg. The higher-frequency modes ν_4 at 724 cm^{-1}, ν_2 at 881 cm^{-1}, ν_1 at 1098 cm^{-1}, and ν_3 at 1442 cm^{-1} represent internal modes of the CO_3^{2-} group. The 229 cm^{-1} frequency external mode and ν_3 (corresponding to the asymmetric CO_3 stretching with E_g symmetry) was not analyzed due to the low intensity and highly asymmetric nature of peak, respectively. The high-frequency mode at 1759 cm^{-1} represents the $2\nu_2$ overtone mode of the ν_2 mode (Couture 1947).

High-pressure experiments

The frequency evolution of carbonate modes as a function of pressure is reported in Figure 2 and the relative changes in frequency $\delta\nu_i/\delta P$ along with literature values in Table 2. The values of $\delta\nu_i/\delta P$ for all modes are quasi-constant over the observed pressure range. Pressure-induced shifts of internal modes are generally less prominent than those of the external modes due to the greater incompressibility of the CO_3 units (Ross and Reeder 1992; Gillet et al. 1993).

In aragonite, the frequencies of all traced modes, except the 145 cm^{-1} external mode, increase monotonously with pressure. Most $\delta\nu_i/\delta P$ values are in good agreement with previous experimental data from Gillet et al. (1993), except for the 182 and 274 cm^{-1} external modes. For these Raman bands, Gillet et al. (1993) may have reported the evolution of multiple vibrational modes, as this could explain the difference between our values and theirs. A similar trend is observed for the frequencies of all traced modes in calcite, except the 1751 cm^{-1} overtone mode, which exhibits a frequency decrease with pressure. The abrupt changes observed between ~1.6 and ~2.1 GPa are attributed to the well-known structural transitions of calcite I to calcite II, which is a reversible first-order ferroelastic transition (Archer et al. 2003), and calcite II to calcite III, which occur at 1.4 and 1.7 GPa, respectively (Bridgman 1938). Above these transition pressures, due to the large number of low-intensity, low-frequency peaks (Pippinger et al. 2015), only data for the most intense peaks resulting from the splitting of the 1088 cm^{-1} peak are presented. These four peaks observed at 1079, 1086, 1098, and 1102 cm^{-1} (at 2.3 GPa) change frequency with a $\delta\nu_i/\delta P$ of 3.15(6), 3.21(6), 3.5(2), and 3.0(1) cm^{-1}/GPa, respectively. A detailed account of the evolution of other calcite modes is given by Pippinger et al. (2015). In dolomite, magnesite, rhodochrosite, and siderite, all traced modes increase in frequency with pressure, except the 881 cm^{-1} internal mode and 1759 cm^{-1} overtone mode in dolomite, the 1727 cm^{-1} overtone mode in rhodochrosite, and the 507 cm^{-1} Fe^{2+} electronic excitation mode and the 1724 cm^{-1} overtone mode in siderite.

High-temperature experiments

The frequency evolution of carbonate modes as a function of temperature is reported in Figure 3 and the relative changes in frequency $\delta\nu_i/\delta T$ along with literature values in Table 2. The values of $\delta\nu_i/\delta T$ of all modes are quasi-constant over the observed temperature range. Temperature-induced shifts of internal modes are generally less prominent than those of the external modes due to the rigidity of C-O bonds in the CO_3 units (Markgraf and Reeder 1985; Reeder and Markgraf 1986; Gillet et al. 1993).

In aragonite, all traced modes except the 701 and 705 cm^{-1} internal modes decrease in frequency with temperature. Above 250 °C, these two modes merge and were treated as one and the neighboring 716 cm^{-1} internal mode no longer appears in spectra. The 164 cm^{-1} external mode is present as a shoulder of the 155 cm^{-1} external mode and could only be traced up to 225 °C. The 216, 250, 263, and 274 cm^{-1} external modes could only be traced up to 200 °C, above which temperature they merge into one broad peak and become indistinguishable from one another. The spectral modifications observed between 425 and 450 °C in Figure 2 are attributed to the aragonite-calcite structural phase transition, which is thermally activated and has been reported to occur at 385 °C (Parker et al. 2010) and 468 °C (Antao and Hassan 2010). In calcite, all traced Raman bands decrease in frequency with temperature. The values of $\delta\nu_i/\delta T$ for all modes in calcite, which has not undergone transformation are lower than those measured from calcite that has formed upon the aragonite-calcite transition. These values are reported in Table 3 along with the corresponding isobaric equivalents of Grüneisen parameter. In dolomite, magnesite, rhodochrosite, and siderite, all traced modes decrease in frequency with temperature, except the 718 cm^{-1} internal mode in rhodochrosite, and the 183 cm^{-1} external mode and the 507 cm^{-1} Fe^{2+} electronic excitation mode in siderite. Thermal decomposition of rhodochrosite was observed between 400 and 425 °C, marked by the sudden disappearance of all its Raman bands. This result is consistent with an XRD study carried out by Kissinger et al. (1956). The 507 cm^{-1} frequency feature in siderite is relatively weak and has the largest $\delta\nu_i/\delta T$ value, but could only be traced up to 250 °C, at which point no longer appears clearly above the background. Popkov et al. (1972) managed to trace this mode from 4.2 K, at which temperature it occurs at 438 cm^{-1} and Langille and O'Shea (1977) from 6 K to room temperature and found that above the Néel temperature its $\delta\nu_i/\delta T$ is linear. Thermal decomposition of siderite was observed between 375 and 400 °C, above which temperature its vibrational modes can no longer be detected. These temperature values are in good agreement with those found in earlier XRD experiments (Kissinger et al. 1956).

Grüneisen and anharmonic parameters

The mode Grüneisen parameter, γ_i, is a dimensionless quantity that links the change in frequency of mode i, ν_i (measured at 25 °C), to the change in volume V (Born and Huang 1954):

$$\gamma_i = -\frac{d\ln\nu_i}{d\ln V} = -\frac{V d\nu_i}{\nu_i dV}$$

Downloaded from https://pubs.geoscienceworld.org/msa/ammin/article-pdf/103/12/1988/4574485/am-2018-6442.pdf
by University of Arizona user
on 17 December 2018

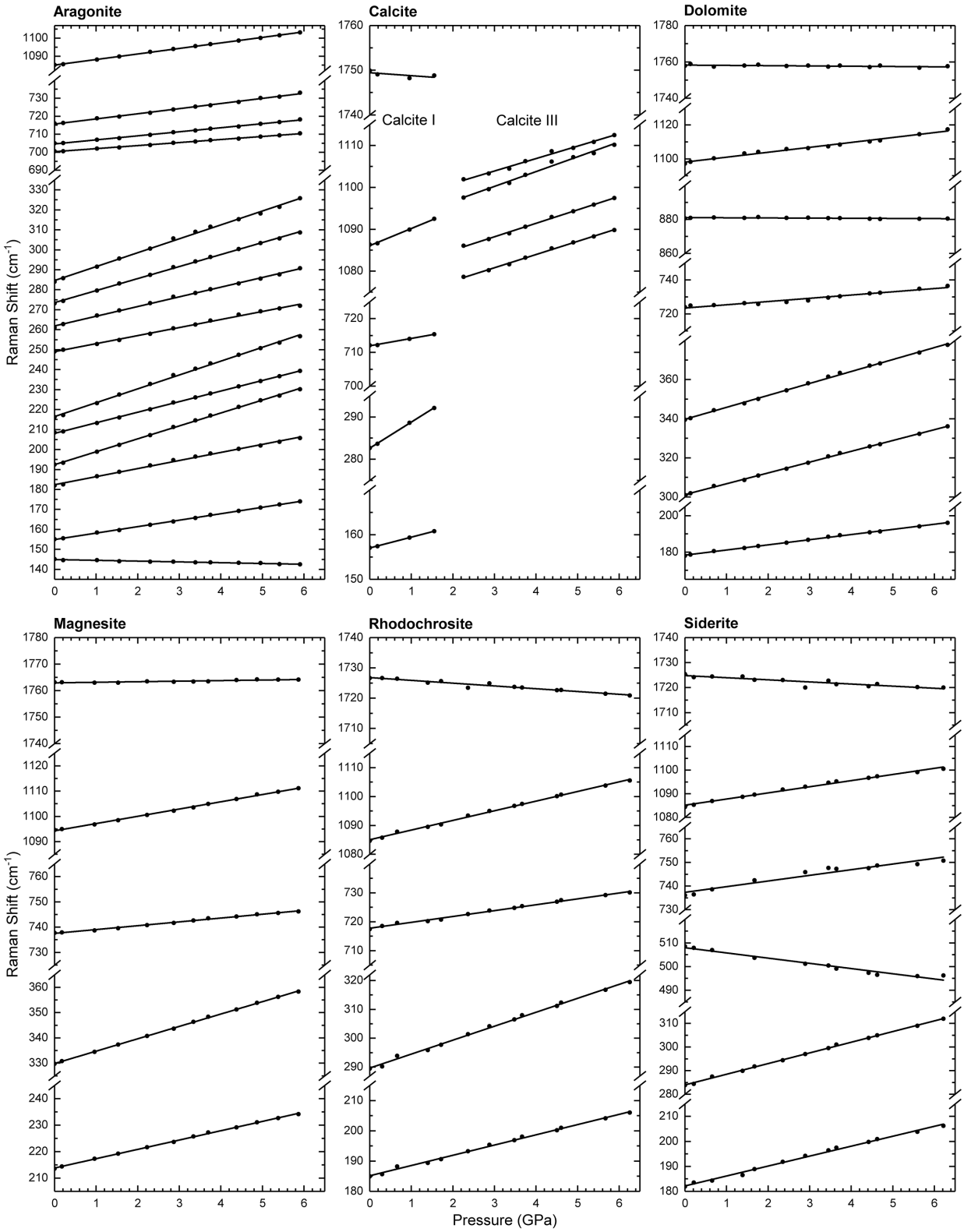

FIGURE 2. Frequency evolution of the traced vibrational modes of carbonates as a function of pressure. The experimental uncertainty lies within the size of the symbol. In the calcite experiment, no data points in the calcite II stability field (situated between calcite I and calcite III stability fields) have been collected.

Downloaded from https://pubs.geoscienceworld.org/msa/ammin/article-pdf/103/12/1988/4574485/am-2018-6442.pdf
by University of Arizona user
on 17 December 2018

TABLE 2. Pressure- and temperature-induced shifts, isobaric and isothermal equivalents of the Grüneisen parameter, and anharmonic parameters of carbonate minerals

Observed mode	Symmetry[a]	ν_i (cm^{-1})	$\delta\nu_i/\delta P$ (cm^{-1}/GPa)	$\delta\nu_i/\delta T$ (cm^{-1}/K)	γ_{iT}[b]	γ_{iP}[c]	a_i ($\times10^{-5}$ K^{-1})	Reference
				Aragonite				
External	B_{1g}	115	?	$-3.1(1)\times10^{-2}$	?	4.10	?	This work
External	B_{3g}	125	?	?	?	?	?	This work
External	A_g	145	−0.40(3)	$-9(2)\times10^{-3}$	−0.19	0.94	−7.30	This work
External	B_{1g}	155	3.23(3)	$-1.9(1)\times10^{-2}$	1.44	1.93	−3.21	This work
		152	2.7(2)					Kraft et al. 1991
		155	$3.0(3)-5(2)\times10^{-4}$	$-2.7(3)\times10^{-2}$	1.2	2.7	−7.2	Gillet et al. 1993
External	A_g	164	?	$-3.9(3)\times10^{-2}$	?	3.65	?	This work
External	B_{2g}	182	4.04(7)	$-1.9(2)\times10^{-2}$	1.53	1.58	−0.29	This work
		180	3.4(6)					Kraft et al. 1991
		180	$7.2(3)-4.7(4)\times10^{-3}$	$-2.4(3)\times10^{-2}$	2.6	2.1	3.4	Gillet et al. 1993
External	B_{3g}	192	6.47(5)	$-1.5(1)\times10^{-2}$	2.32	1.23	7.11	This work
External	B_{2g}	208	5.30(3)	$-3.49(6)\times10^{-2}$	1.75	2.58	−5.35	This work
		206	3.3(5)					Kraft et al. 1991
		209	4.0(4)	$-4.1(4)\times10^{-2}$	1.2	3.0	−11.6	Gillet et al. 1993
External	A_g	216	6.94(9)	$-2.5(2)\times10^{-2}$	2.21	1.77	2.88	This work
		217	$6.6(4)-3.3(3)\times10^{-3}$					Gillet et al. 1993
External	B_{2g}	250	4.03(6)	$-2.7(2)\times10^{-2}$	1.11	1.66	−3.57	This work
		254	?	$-2.0(3)\times10^{-2}$				Gillet et al. 1993
External	B_{2g}	263	4.79(6)	$-4.5(2)\times10^{-2}$	1.27	2.64	−8.90	This work
External	B_{3g}	274	6.02(5)	$-3.40(6)\times10^{-2}$	1.51	1.91	−2.56	This work
		275	3.4(3)					Gillet et al. 1993
External	A_g	285	7.0(1)	$-2.9(1)\times10^{-2}$	1.68	1.57	0.76	This work
Internal ν_4	B_{3g}	701	1.69(3)	$5.3(6)\times10^{-3}$	0.17	−0.12	1.84	This work
		704	1.5(1)					Kraft et al. 1991
		702	1.6(3)	0	0.14	0.0	0.9	Gillet et al. 1993
Internal ν_4	A_g	705	2.25(3)	$2.6(6)\times10^{-3}$	0.22	−0.06	1.80	This work
		710	2.0(3)	$-1.5(3)\times10^{-2}$	0.20	0.3	−0.9	Gillet et al. 1993
Internal ν_4	B_{2g}	716	2.85(5)	$-4(2)\times10^{-3}$	0.27	0.09	1.17	This work
Internal ν_2	A_g	853	?	$-2.4(7)\times10^{-3}$	?	0.04	?	This work
Internal ν_1	A_g	1085	3.07(2)	$-1.32(7)\times10^{-2}$	0.20	0.19	0.06	This work
		1086	2.3(1)					Kraft et al. 1991
		1084	2.7(3)	$-1.5(2)\times10^{-2}$	0.16	0.21	−0.2	Gillet et al. 1993
Internal ν_3	B_{1g}	1463	?	$-2.6(1)\times10^{-2}$	?	0.27	?	This work
		1463	?	$-2.2(3)\times10^{-2}$				Gillet et al. 1993
Internal ν_3	B_{2g}	1576	?	$-3.3(3)\times10^{-2}$	?	0.32	?	This work
		1575	?	$-3.1(3)\times10^{-2}$				Gillet et al. 1993
				Calcite				
External	E_g	158	2.42(4)	$-2.65(2)\times10^{-2}$	1.16	18.61	−15.71	This work
		156	2.47		1.18(6)			Liu and Mernagh 1990
		156	2.3(3)	$-2.8(3)\times10^{-2}$	1.2	19.9	−16.9	Gillet et al. 1993
		156	2.52(8)		1.14(4)			Liu et al. 2016
External	E_g	284	6.2(1)	$-4.30(4)\times10^{-2}$	1.65	16.85	−13.68	This work
		283	5.27		1.38(8)			Liu and Mernagh 1990
		281	6.0(5)	$-4.0(3)\times10^{-2}$	1.4	15.8	−13.0	Gillet et al. 1993
		282	5.19(17)		1.33(6)			Liu et al. 2016
Internal ν_4	E_g	713	2.2(1)	$-5.0(2)\times10^{-3}$	0.23	0.77	−0.48	This work
		713	2.22		0.24			Liu and Mernagh 1990
		711	1.7(3)	$-4(1)\times10^{-3}$	0.23	0.62	−0.3	Gillet et al. 1993
		713	2.35(7)		0.23(1)			Liu et al. 2016
Internal ν_1	A_{1g}	1088	4.1(2)	$-9.7(3)\times10^{-3}$	0.29	0.99	−0.63	This work
		1085	5.87		0.41(1)			Liu and Mernagh 1990
		1085	3.0(3)	$-4.0(2)\times10^{-3} - 1.40(5)\times10^{-5}$	0.40	0.51	−0.1	Gillet et al. 1993
		1086	5.96(15)		0.39(2)			Liu et al. 2016
Internal ν_3	E_g	1438	?	?	?	?	?	This work
		1434	9.0		0.47(3)			Liu and Mernagh 1990
		1434	7.5(5)	$-2.5(3)\times10^{-2} + 2.9(3)\times10^{-5}$	0.46	1.94	−1.3	Gillet et al. 1993
Overtone		1751	−0.7(5)	$-1.36(6)\times10^{-2}$	−0.03	0.86	−0.80	This work
		1748	−1.0(4)	$-5.3(5)\times10^{-3} - 2.3(2)\times10^{-5}$	−0.04	0.34	−0.34	Gillet et al. 1993
				Dolomite				
External	E_g	178	2.83(3)	$-1.65(8)\times10^{-2}$	1.50	3.84	−5.65	This work
		177	1.4(2)					Kraft et al. 1991
		178	1.8(2)	$-1.9(2)\times10^{-2} - 3.5(3)\times10^{-6}$	0.9	4.4	−8.4	Gillet et al. 1993
External	A_g	229	?	?	?	?	?	This work
External	E_g	301	5.53(5)	$-3.60(9)\times10^{-2}$	1.73	4.95	−7.78	This work
		301	4.4(3)					Kraft et al. 1991
		300	4.4(3)	$-3.2(3)\times10^{-2} - 1.96(5)\times10^{-5}$	1.4	4.4	−7.3	Gillet et al. 1993
External	A_g	340	6.11(7)	$-4.7(3)\times10^{-2}$	1.69	5.73	−9.73	This work
		335	2.9(2)	$-1.9(2)\times10^{-2} - 7.8(5)\times10^{-5}$	0.8	2.3	−3.7	Gillet et al. 1993
Internal ν_4	E_g	724	1.9(1)	$-2.8(9)\times10^{-3}$	0.25	0.16	0.21	This work
		725	1.1(2)					Kraft et al. 1991
		724	1.6(3)	$-2.1(5)\times10^{-3} - 1.7(3)\times10^{-5}$	0.2	0.12	0.2	Gillet et al. 1993
Internal ν_2	A_g	881	−0.10(4)	$-4.2(9)\times10^{-3}$	−0.01	0.20	−0.50	This work
		880	?	0				Gillet et al. 1993

(Table continues on next page)

Downloaded from https://pubs.geoscienceworld.org/msa/ammin/article-pdf/103/12/1988/4574485/am-2018-6442.pdf
by University of Arizona user
on 17 December 2018

TABLE 2.—*CONTINUED*

Observed mode	Symmetry[a]	ν_i (cm^{-1})	$\delta\nu_i/\delta P$ (cm^{-1}/GPa)	$\delta\nu_i/\delta T$ (cm^{-1}/K)	γ_{iT}[b]	γ_{iP}[c]	a_i ($\times10^{-5}$ K^{-1})	Reference
				Dolomite (cont'd)				
Internal ν_1	A_g	1098	2.9(1)	$-6(1)\times10^{-3}$	0.25	0.24	0.03	This work
		1101	3.5(3)					Kraft et al. 1991
		1097	2.9(3)	$-6.4(4)\times10^{-3} - 1.6(3)\times10^{-5}$	0.25	0.24	0.0	Gillet et al. 1993
Internal ν_3	E_g	1442	?	?	?	?	?	This work
		1439	3.5(3)	$-3.5(3)\times10^{-2} + 4.1(2)\times10^{-5}$	0.23	1.01	−1.9	Gillet et al. 1993
Overtone		1759	−0.15(6)	$-1.5(1)\times10^{-2}$	−0.01	0.35	−0.87	This work
		1750	−0.79(5)	$-1.3(2)\times10^{-3} - 1.60(4)\times10^{-5}$	−0.02	0.03	−0.1	Gillet et al. 1993
				Magnesite				
External	E_g	214	3.52(3)	$-2.05(5)\times10^{-2}$	1.76	4.95	−6.16	This work
		216	2.6(2)		1.4(1)			Williams et al. 1992
		213	$4.6(4) - 4.4(3)\times10^{-3}$	$-9(2)\times10^{-3} - 2.6(2)\times10^{-5}$	2.6	2.4	0.3	Gillet et al. 1993
External	E_g	330	4.89(3)	$-3.01(5)\times10^{-2}$	1.59	4.73	−6.07	This work
		329	4.7(1)		1.67(4)			Williams et al. 1992
		329	4.5(3)	$-1.9(3)\times10^{-2} - 2.5\times10^{-5}$	1.7	3.0	−2.5	Gillet et al. 1993
Internal ν_4	E_g	738	1.52(4)	$-2.0(8)\times10^{-3}$	0.22	0.14	0.16	This work
		735	1.5(2)		0.24(3)			Williams et al. 1992
		738	1.4(2)	0	0.23	0.00	0.44	Gillet et al. 1993
Internal ν_1	A_{1g}	1094	2.87(4)	$-1.4(7)\times10^{-3}$	0.28	0.07	0.41	This work
		1095	2.3(1)		0.24(2)			Williams et al. 1992
		1094	2.5(3)	$-3.5(3)\times10^{-3} - 3.1(2)\times10^{-5}$	0.28	0.17	0.21	Gillet et al. 1993
Internal ν_3	E_g	1446	?	?	?	?	?	This work
		1444	4.0(4)	$-3.0(3)\times10^{-2} + 5.5(2)\times10^{-5}$	0.34	1.08	−1.42	Gillet et al. 1993
Overtone		1763	0.21(3)	$-1.63(8)\times10^{-2}$	0.01	0.48	−0.90	This work
		1762	−0.42(4)	$-2.6(3)\times10^{-2}$	−0.03	0.76	−1.52	Gillet et al. 1993
				Rhodochrosite				
External	E_g	185	3.38(6)	$-1.98(6)\times10^{-2}$	2.09	4.63	−5.81	This work
		201	2.685					Farfan et al. 2013
		184	2.91(5)		2.37(7)			Liu et al. 2016
External	E_g	290	4.83(8)	$-2.93(6)\times10^{-2}$	1.90	4.43	−5.76	This work
		302	4.147					Farfan et al. 2013
		290	3.68(9)		1.99(8)			Liu et al. 2016
Internal ν_4	E_g	718	2.03(4)	$1.4(8)\times10^{-3}$	0.32	−0.09	0.95	This work
		723	0.946					Farfan et al. 2013
		719	1.28(6)		0.33(3)			Liu et al. 2016
Internal ν_1	A_{1g}	1086	3.34(5)	$-5.8(7)\times10^{-3}$	0.35	0.22	0.29	This work
		1100	1.906					Farfan et al. 2013
		1086	2.17(7)		0.38(3)			Liu et al. 2016
Internal ν_3	E_g	1415	?	?	?	?	?	This work
Overtone		1727	−0.92(7)	$-1.3\ (1)\times10^{-2}$	−0.06	0.31	−0.85	This work
				Siderite				
External	E_g	183	3.98(9)	$1(1)\times10^{-3}$	2.54	−0.17	7.29	This work
External	E_g	284	4.52(5)	$-1.0(1)\times10^{-2}$	1.86	1.31	1.49	This work
		299	3.74					Farfan et al. 2012
Fe^{2+} electronic excitation		507	−2.2(1)	0.130(4)	−0.51	−9.55	24.32	This work
Internal ν_4	E_g	731	2.4(2)	$-1.35(9)\times10^{-2}$	0.38	0.68	−0.81	This work
Internal ν_1	A_{1g}	1085	2.60(7)	$-3(1)\times10^{-3}$	0.28	0.10	0.48	This work
		1088	2.20					Farfan et al. 2012
Overtone		1724	−0.8(1)	$-1.6(1)\times10^{-2}$	−0.06	0.35	−1.10	This work

Notes: The values of ν_i were measured at ambient pressure and temperature (in this work, 1 bar and 25 °C).

[a] Symmetry of the modes are from: aragonite (De La Pierre et al. 2014), dolomite (Valenzano et al. 2007), calcite, magnesite, rhodochrosite, and siderite (Rutt and Nicola 1974).

[b] The isothermal equivalent of the Grüneisen parameter was calculated with the following bulk moduli: aragonite 68.9 GPa (Liu et al. 2005), calcite 76.1 GPa (Chen et al. 2001), dolomite 94 GPa (Ross and Reeder 1992), magnesite 107 GPa (Zhang and Reeder 1999), rhodochrosite 114.3 GPa (Chen et al. 2001), and siderite 117 GPa (Zhang and Reeder 1999).

[c] The isobaric equivalent of the Grüneisen parameter was calculated with the following thermal expansion coefficients: aragonite 6.5×10^{-5} K^{-1} (Ye et al. 2012), calcite 0.9×10^{-5} K^{-1} (Markgraf and Reeder 1985), dolomite 2.41×10^{-5} K^{-1} (Reeder and Markgraf 1986), magnesite 1.93×10^{-5} K^{-1} (Markgraf and Reeder 1985), rhodochrosite 2.28×10^{-5} K^{-1} (Krishna Rao and Satyanaryana Murthy 1970), and siderite 2.69×10^{-5} K^{-1} (Pfaff cited in Mellor 1935).

Its isobaric equivalent, γ_{iP} (Gillet et al. 1989) can be expressed as:

$$\gamma_{iP} = -\frac{d\ln\nu_i}{d\ln V(T)} = -\frac{d\nu_i}{\alpha\nu_i dT}$$

where α is the thermal expansion coefficient. Its isothermal equivalent, γ_{iT} (Gillet et al. 1989; Wagner 2000) can be expressed as:

$$\gamma_{iT} = -\frac{d\ln\nu_i}{d\ln V(P)} = \frac{K_T d\nu_i}{\nu_i dP}$$

where K_T is the isothermal bulk modulus.

From γ_{iT} and γ_{iP}, the intrinsic anharmonic parameter, a_i, can be calculated for each mode (Gillet et al. 1989):

$$a_i = \alpha(\gamma_{iT} - \gamma_{iP})$$

The isobaric and isothermal equivalents of the Grüneisen parameter and the anharmonic parameter have been calculated for each studied mode and are presented in Table 2.

There is noticeable variation in published ν_i, $\delta\nu_i/\delta P$, $\delta\nu_i/\delta T$, and, consequently, γ_{iT}, γ_{iP}, and a_i values corresponding to the

Downloaded from https://pubs.geoscienceworld.org/msa/ammin/article-pdf/103/12/1988/4574485/am-2018-6442.pdf
by University of Arizona user
on 17 December 2018

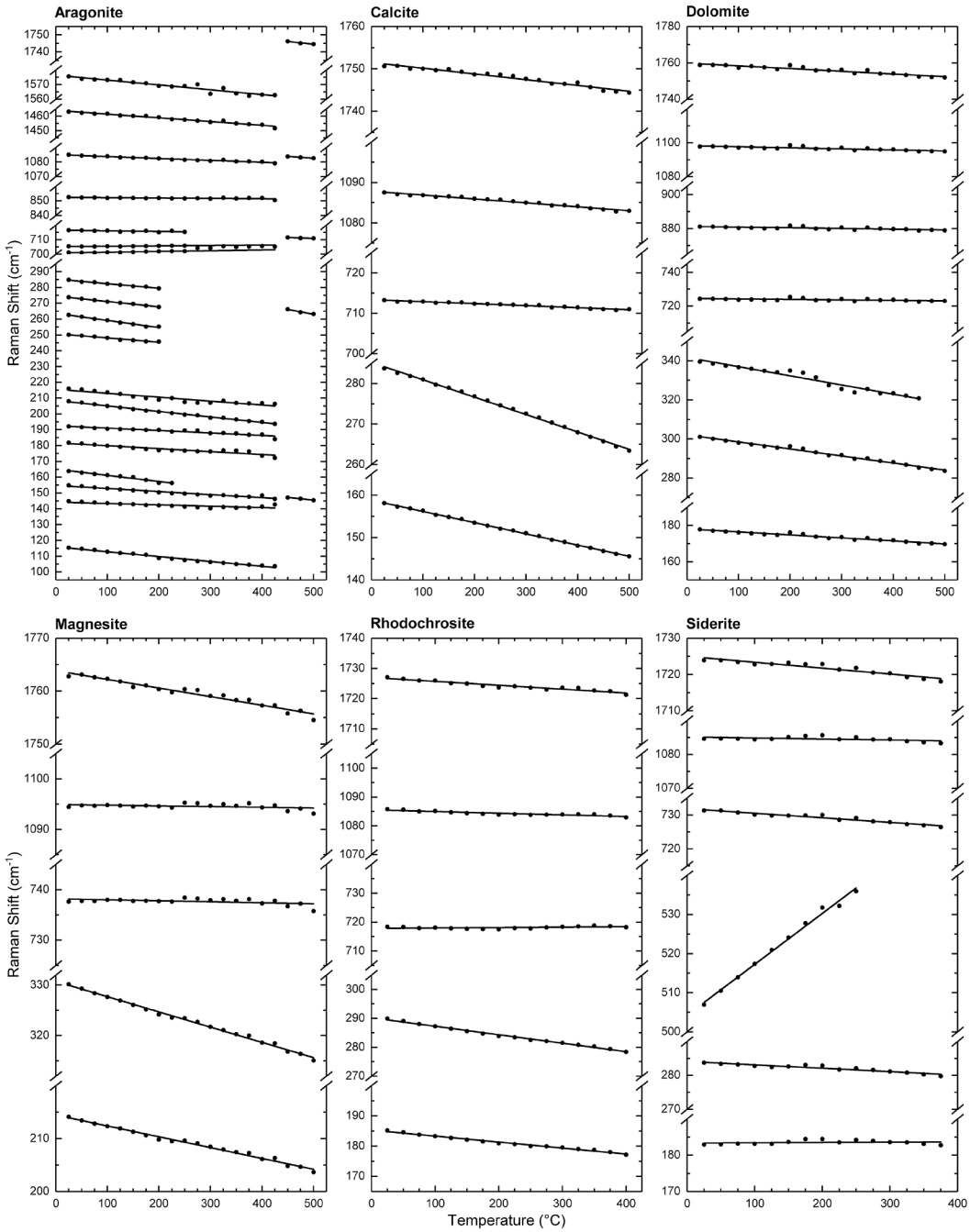

FIGURE 3. Frequency evolution of the traced vibrational modes of carbonates as a function of temperature. The experimental uncertainty lies within the size of the symbol.

same Raman-active modes of any particular carbonate mineral. The primary reason for this variation is probably trace element content. Owing to the difference in ion size (Mg^{2+}, Mn^{2+}, and Fe^{2+} are significantly smaller than Ca^{2+}), substitution with a smaller ion will decrease the average interatomic distances and increase the frequency of external modes (Krishnamurti 1956; Rutt and Nicola 1974). As CaO_6 octahedra are slightly more compressible than MgO_6 and FeO_6 octahedra (Ross and Reeder 1992), trace element content will also affect $\delta\nu_i/\delta P$ values. Due to the variable and more complex effects of temperature on the structure of carbonates with different ions (e.g., Markgraf and Reeder 1985; Reeder and Markgraf 1986), non-end-member compositions will exhibit a range of $\delta\nu_i/\delta T$ values, too.

Development of a *P-T* calibrant

The Raman data presented above allow us to develop a *P-T* calibrant for each of the carbonate phases on the basis of the measured frequencies of each of their Raman-active modes.

Downloaded from https://pubs.geoscienceworld.org/msa/ammin/article-pdf/103/12/1988/4574485/am-2018-6442.pdf
by University of Arizona user
on 17 December 2018

TABLE 3. Temperature induced shifts and isobaric equivalents of the Grüneisen parameter of calcite and calcite after aragonite-calcite transition

Observed mode	Symmetry	ν_i (cm^{-1}) Calcite	$\delta\nu_i/\delta T$ (cm^{-1}/K) Calcite after Aragonite	$\delta\nu_i/\delta T$ (cm^{-1}/K) Calcite	γ_{iP}[a] Calcite after Aragonite	γ_{iP}[a]
External	E_g	158	$-2.65(2)\times10^{-2}$	$-3.4(2)\times10^{-2}$	18.61	23.60
External	E_g	284	$-4.30(4)\times10^{-2}$	$-6.1(7)\times10^{-2}$	16.85	24.02
Internal ν_4	E_g	713	$-5.0(2)\times10^{-3}$	$-1.1(4)\times10^{-2}$	0.77	1.67
Internal ν_1	A_{1g}	1088	$-9.7(3)\times10^{-3}$	$-2.40(2)\times10^{-2}$	0.99	2.45
Overtone		1751	$-1.36(6)\times10^{-2}$	$-3.3(9)\times10^{-2}$	0.86	2.10

[a] The isobaric equivalent of the Grüneisen parameter was calculated with a calcite thermal expansion coefficient of 0.9×10^{-5} K^{-1} (Markgraf and Reeder 1985).

The separate impacts of pressure and temperature on each of the modes, and their subtle differences provide a robust route to identifying the temperature and pressure conditions within the DAC assembly, based on the set of measured Raman peaks for each sample.

As the pressure and temperature cross derivative of the frequency is negligible (Matas et al. 2000), the frequency ν_{PTi} of mode *i* at any *P-T* condition (in the experimental range) can be expressed as

$$\nu_{PTi} = \nu_{0i} + P\frac{d\nu_i}{dP} + T\frac{d\nu_i}{dT}$$

where ν_{0i} is the extrapolated frequency of mode *i* at ambient pressure and zero temperature.

In an experiment carried out at a known temperature, *T* (e.g., measured by a thermocouple), pressure can be determined based on the measured ν_{PTi} of a single mode. If ν_{PTi} of multiple modes are measured, pressure can be most accurately determined by the simple linear regression method. We have tested our method by determining pressure and temperature for a cell loaded with rhodochrosite and employing the frequencies of the 185, 290, 1086, and 1415 cm^{-1} modes of rhodochrosite. The cell was held at 300 °C as set temperature and experiments were conducted at two separate pressures. In our experiment, this method gave 1.2(1) and 1.4(3) GPa for two determinations at pressure 1 and 4.7(1) and 4.9(1) GPa for two at pressure 2, while *T* was fixed to the value determined by thermocouple, measured to be 300 °C. In an experiment carried out at unknown pressure *P* and temperature *T*, these variables can be determined based on measured ν_{PTi} of two or more modes. If ν_{PTi} of more than two modes are measured, pressure and temperature can be determined by a multiple linear regression method. In our experiment, using rhodochrosite as pressure and temperature sensor, this method gave 1.2(1) and 1.4(4) GPa at pressure 1 and 4.6(1) and 4.8(2) GPa at pressure 2 with the temperature also determined by fit to the *P-T* dependence of all modes and calculated as 293(8) °C, which is equal to the value determined by thermocouple to within the stated error.

In general, the most suitable modes are those with high peak intensity, high sensitivity to pressure and temperature changes, with an anharmonic parameter close to 0 and with γ_{iT} and γ_{iP} similar to each other. The latter two features are indicative of quasi-harmonic behavior, where pressure and temperature affect the vibration frequencies only through the volume changes and not by modifications of the electronic structure of the chemical bond involved (Gillet et al. 1989). As mentioned above, trace element content could affect ν_i, $\delta\nu_i/\delta P$, and $\delta\nu_i/\delta T$ for carbonate modes, particularly those of external modes. This important factor should also be taken into consideration when choosing the most suitable modes for *P-T* determination. It is safest to carry out independent *P-T* calibration against ruby or another pressure sensor, when dealing with impure samples, to overcome the uncertainty arising from carbonate composition.

In aragonite, the internal ν_1 mode is most suitable for *P-T* determination (Facq et al. 2014, 2016), followed by the external modes, in decreasing order of priority: 155, 208, 182, 192, 216, 145, 250, 263, 274, and 285 cm^{-1}. In calcite, dolomite, magnesite, rhodochrosite, and siderite the preferred use of the internal ν_1 mode is recommended, followed by the external modes and the overtone mode. The external modes, in decreasing order of priority, should be used as follows: in calcite, 284 and 158 cm^{-1}; in dolomite, 301, 178, and 340 cm^{-1}; in magnesite, 330 and 214 cm^{-1}; in rhodochrosite, 290 and 185 cm^{-1}; and in siderite, 284 and 183 cm^{-1}.

It is worth noting that the widths of Raman peaks have previously been proposed as a proxy for temperature (Gillet et al. 1993). The reported errors in temperature for this approach are generally larger than those for temperatures obtained from peak positions. Additionally, instrumental peak broadening makes this method dependent (to a greater extent than peak positions) on the experimental setup in the laboratory within which analyses are conducted. Furthermore, the influence of combined pressure and temperature on peak widths is significantly more complicated than their impact on peak positions alone. For these reasons, we have chosen not to make use of any additional information encoded into the peak widths of our measured carbonate Raman-active modes.

Our *P-T* determination method has limited use in calcite high *P-T* experiments. In the case of calcite II and calcite III $CaCO_3$ polymorphs, $\delta\nu_i/\delta T$ is not measurable at ambient pressure because of the location of stability fields of these phases. For this reason, a simultaneous *P-T* determination is not possible based on the Raman-active modes of these phases, and our method is limited to pressure determination at known (measured) temperature.

IMPLICATIONS

From our results, it can be seen that pressure- and temperature-induced frequency shifts in aragonite, calcite, dolomite, magnesite, rhodochrosite, and siderite all provide a sensitive and robust alternative to traditional pressure calibrants (e.g., ruby, diamond) in diamond-anvil cell (DAC) experiments, and this is especially useful when any such external traditional calibrant might contaminate the pressure-transmitting media due to their increased solubility at high *P-T* conditions (Manning 1994; Datchi et al. 2000; Tropper and Manning 2007; Watenphul and Schmidt 2012; Andreani et al. 2013). As they do not interfere with the primary measurement, our carbonate calibrants represent an alternative for *P-T* measurement in a wide range of DAC experiments addressing carbonate solubility and/or aqueous speciation at high *P-T* conditions relevant to the Earth's crust and mantle

Downloaded from https://pubs.geoscienceworld.org/msa/ammin/article-pdf/103/12/1988/4574485/am-2018-6442.pdf
by University of Arizona user
on 17 December 2018

to better constrain the Earth's deep carbon cycle. The measured pressure- and temperature-induced frequency shifts have been used to calculate the isobaric and isothermal equivalents of the Grüneisen parameter and the anharmonic parameter. This could be used for the anharmonic correction of specific heat capacity at constant volume, which is responsible for the departure from the Dulong-Petit limit at high temperature (Gillet et al. 1989). The anharmonic correction also helps to refine thermodynamic properties and phase equilibriums at high pressure and temperature conditions.

Acknowledgments

The Sedgwick Museum of Earth Sciences, University of Cambridge, is acknowledged for dolomite, rhodochrosite, and siderite samples. Daniel Ozdín is acknowledged for the magnesite sample. Giulio I. Lampronti and Iris Buisman are acknowledged for their assistance with XRD and EPMA analysis, respectively. This research was funded by NERC through grant NE/P019714/1 to S.A.T.R. and a NERC DTP studentship to S.F.

References cited

Ague, J.J., and Nicolescu, S. (2014) Carbon dioxide released from subduction zones by fluid-mediated reactions. Nature Geoscience, 7, 355–360.

Andreani, M., Daniel, I., and Pollet-Villard, M. (2013) Aluminum speeds up the hydrothermal alternation of olivine. American Mineralogist, 98, 1738–1744.

Antao, S.M., and Hassan, I. (2010) Temperature dependence of the structural parameters in the transformation of aragonite to calcite, as determined from in situ synchrotron powder X-ray-diffraction data. Canadian Mineralogist, 48, 1225–1236.

Archer, T.D., Birse, S.E.A., Dove, M.T., Redfern, S.A.T., Gale, J.D., and Cygan, R.T. (2003) An interatomic potential model for carbonates allowing for polarization effects. Physics and Chemistry of Minerals, 30, 416–424.

Barnett, J.D., Block, S., and Piermarini, G.J. (1973) An optical fluorescence system for quantitative pressure measurement in the diamond-anvil cell. Review of Scientific Instruments, 44, 1–9.

Bernini, D., Audétat, A., Dolejš, D., and Keppler, H. (2013) Zircon solubility in aqueous fluids at high temperatures and pressures. Geochimica et Cosmochimica Acta, 119, 178–187.

Born, M., and Huang, K. (1954) Dynamical Theory of Crystal Lattices. Clarendon.

Bridgman, P.W. (1938) The high pressure behavior of miscellaneous minerals. American Journal of Science, 237, 7–18.

Cerantola, V., McCammon, C., Kupenko, I., Kantor, I., Marini, C., Wilke, M., Ismailova, L., Solopova, N., Chumakov, A., Pascarelli, S., and others. (2015) High-pressure spectroscopic study of siderite ($FeCO_3$) with a focus on spin crossover. American Mineralogist, 100, 2670–2681.

Chaney, J., Santillán, J.D., Knittle, E., and Williams, Q. (2015) A high-pressure infrared and Raman spectroscopic study of $BaCO_3$: the aragonite, trigonal and *Pmmn* structures. Physics and Chemistry of Minerals, 1, 83–93.

Chariton, S., Cerantola, V., Ismailova, L., Bykova, E., Bykov, M., Kupenko, I., McCammon, C., and Dubrovinsky, L. (2017) The high-pressure behavior of spherocobaltite ($CoCO_3$): a single crystal Raman spectroscopy and XRD study. Physics and Chemistry of Minerals, 45, 59–68.

Chen, C.C., Lin, C.C., Liu, L.G., Sinogeikin, S.V., and Bass, J.D. (2001) Elasticity of single-crystal calcite and rhodochrosite by Brillouin spectroscopy. American Mineralogist, 86, 1525–1529.

Couture, L. (1947) Etude des spectres de vibration de monocristaux ioniques. In Annales de physique. Vol. 12. No. 2, pp. 5–94. EDP Sciences.

Dasgupta, R., and Hirschmann, M.M. (2006) Melting in the Earth's deep upper mantle caused by carbon dioxide. Nature, 440, 659–662.

——— (2010) The deep carbon cycle and melting in Earth's interior. Earth and Planetary Science Letters, 298, 1–13.

Dasgupta, R., Hirschmann, M.M., and Withers, A.C. (2004) Deep global cycling of carbon constrained by the solidus of anhydrous, carbonated eclogite under upper mantle conditions. Earth and Planetary Science Letters, 227, 73–85.

Datchi, F., Loubeyre, P., and LeToullec, R. (2000) Extended and accurate determination of the melting curves of argon, helium, ice (H_2O), and hydrogen (H_2). Physical Review B, 61, 6535–6546.

Datchi, F., Dewaele, A., Loubeyre, P., Letoullec, R., Le Godec, Y., and Canny, B. (2007) Optical pressure sensors for high-pressure–high-temperature studies in a diamond anvil cell. High Pressure Research, 27, 447–463.

De La Pierre, M., Carteret, C., Maschio, L., André, E., Orlando, R., and Dovesi, R. (2014) The Raman spectrum of $CaCO_3$ polymorphs calcite and aragonite: A combined experimental and computational study. The Journal of Chemical Physics, 140, 164509.

Facq, S., Daniel, I., Montagnac, G., Cardon, H., and Sverjensky, D.A. (2014) In situ Raman study and thermodynamic model of aqueous carbonate speciation in equilibrium with aragonite under subduction zone conditions. Geochimica et Cosmochimica Acta, 132, 375–390.

——— (2016) Carbon speciation in saline solutions in equilibrium with aragonite at high pressure. Chemical Geology, 431, 44–53.

Farfan, G., Wang, S., Ma, H., Caracas, R., and Mao, W.L. (2012) Bonding and structural changes in siderite at high pressure. American Mineralogist, 97, 1421–1426.

Farfan, G.A., Boulard, E., Wang, S., and Mao, W.L. (2013) Bonding and electronic changes in rhodochrosite at high pressure. American Mineralogist, 98, 1817–1823.

Gillet, P., Guyot, F., and Malezieux, J.M. (1989) High-pressure, high-temperature Raman spectroscopy of Ca_2GeO_4 (olivine form): some insights on anharmonicity. Physics of the Earth and Planetary Interiors, 58, 141–154.

Gillet, P., Biellmann, C., Reynard, B., and McMillan, P. (1993) Raman spectroscopic studies of carbonates Part I: High-pressure and high-temperature behaviour of calcite, magnesite, dolomite and aragonite. Physics and Chemistry of Minerals, 20, 1–18.

Goncharov, A.F., Zaug, J.M., Crowhurst, J.C., and Gregoryanz, E. (2005) Optical calibration of pressure sensors for high pressures and temperatures. Journal of Applied Physics, 97.

Grasset, O., Amiguet, E., and Choukroun, M. (2005) Pressure measurements within optical cells using diamond sensors: accuracy of the method below 1 GPa. High Pressure Research, 25, 255–265.

Kelemen, P.B., and Manning, C.E. (2015) Reevaluating carbon fluxes in subduction zones, what goes down, mostly comes up. Proceedings of the National Academy of Sciences, 112, E3997–E4006.

Kissinger, H.E., McMurdie, H.F., and Simpson, B.S. (1956) Thermal decomposition of manganous and ferrous carbonates. Journal of the American Ceramic Society, 39, 168–172.

Klotz, S., Chervin, J.C., Munsch, P., and Le Marchand, G. (2009) Hydrostatic limits of 11 pressure transmitting media. Journal of Physics D: Applied Physics, 42, 75,413.

Koch-Müller, M., Jahn, S., Birkholz, N., Ritter, E., and Schade, U. (2016) Phase transitions in the system $CaCO_3$ at high P and T determined by in situ vibrational spectroscopy in diamond anvil cells and first-principles simulations. Physics and Chemistry of Minerals, 43, 545–561.

Kraft, S., Knittle, E., and Williams, Q. (1991) Carbonate stability in the Earth's mantle: A vibrational spectroscopic study of aragonite and dolomite at high pressures and temperatures. Journal of Geophysical Research, 96, 17,997–18,009.

Krishna Rao, K.V., and Satyanaryana Murthy, K. (1970) Thermal expansion of manganese carbonate. Journal of Materials Science, 5, 82–83.

Krishnamurti, D. (1956) Raman spectrum of magnesite. Proceedings of the Indian Academy of Sciences—Section A, 43, 210–212.

——— (1957) The Raman spectrum of calcite and its interpretation. Proceedings of the Indian Academy of Sciences—Section A, 46, 183–202.

Langille, D.B., and O'Shea, D.C. (1977) Raman spectroscopy studies of antiferromagnetic $FeCO_3$ and related carbonates. Journal of Physics and Chemistry of Solids, 38, 1161–1171.

Letoullec, R., Pinceaux, J.P., and Loubeyre, P. (1988) The membrane diamodn anvil cell: A new device for generating continuous pressure and temperature variations. High Pressure Research, 1, 77–90.

Lin, C.C., and Liu, L.G. (1997) High pressure phase transformations in aragonite-type carbonates. Physics and Chemistry of Minerals, 24, 149–157.

Liu, L.G., and Mernagh, T.P. (1990) Phase transitions and Raman spectra of calcite at high pressures and room temperature. American Mineralogist, 75, 801–806.

Liu, L.G., Chen, C.C., Lin, C.C., and Yang, Y.J. (2005) Elasticity of single-crystal aragonite by Brillouin spectroscopy. Physics and Chemistry of Minerals, 32, 97–102.

Liu, J., Caracas, R., Fan, D., Bobocioiu, E., Zhang, D., and Mao, W.L. (2016) High-pressure compressibility and vibrational properties of $(Ca,Mn)CO_3$. American Mineralogist, 101, 2723–2730.

Manning, C.E. (1994) The solubility of quartz in H_2O in the lower crust and upper mantle. Geochimica et Cosmochimica Acta, 58, 4831–4839.

——— (2014) A piece of the deep carbon puzzle. Nature Geoscience, 7, 333–334.

Mao, H.K., Xu, J., and Bell, P.M. (1986) Calibration of the ruby pressure gauge to 800 kbar under quasi-hydrostatic conditions. Journal of Geophysical Research, 91, 4673–4676.

Markgraf, S.A., and Reeder, R.J. (1985) High-temperature structure refinements of calcite and magnesite. American Mineralogist, 70, 590–600.

Maruyama, K., Kagi, H., Komatsu, K., Yoshino, T., and Nakano, S. (2017) Pressure-induced phase transitions of vaterite, a metastable phase of $CaCO_3$. Journal of Raman Spectroscopy, 48, 1449–1453.

Matas, J., Gillet, P., Ricard, Y., and Martinez, I. (2000) Thermodynamic properties of carbonates at high pressures from vibrational modelling. European Journal of Mineralogy, 12, 703–720.

Mellor, J.W. (1935) A Comprehensive Treatise on Inorganic and Theoretical Chemistry. Vol. XIV: Fe (Part III), Co, 892 p. Longmans.

Minch, R., Seoung, D.H., Ehm, L., Winkler, B., Knorr, K., Peters, L., Borkowski,

Downloaded from https://pubs.geoscienceworld.org/msa/ammin/article-pdf/103/12/1988/4574485/am-2018-6442.pdf
by University of Arizona user
on 17 December 2018

L.A., Parise, J.B., Lee, Y., Dubrovinsky, L., and others. (2010a) High-pressure behavior of otavite ($CdCO_3$). Journal of Alloys and Compounds, 508, 251–257.

Minch, R., Dubrovinsky, L., Kurnosov, A., Ehm, L., Knorr, K., and Depmeier, W. (2010b) Raman spectroscopic study of $PbCO_3$ at high pressures and temperatures. Physics and Chemistry of Minerals, 37, 45–56.

Müller, J., Speziale, S., Efthimiopoulos, I., Jahn, S., and Koch-Müller, M. (2016) Raman spectroscopy of siderite at high pressure: Evidence for a sharp spin transition. American Mineralogist, 101, 2638–2644.

Oganov, A.R., Hemley, R.J., Hazen, R.M., and Jones, A.P. (2013) Structure, bonding, and mineralogy of carbon at extreme conditions. Reviews in Mineralogy and Geochemistry, 75, 47–77.

Parker, J.E., Thompson, S.P., Lennie, A.R., Potter, J., and Tang, C.C. (2010) A study of the aragonite-calcite transformation using Raman spectroscopy, synchrotron powder diffraction and scanning electron microscopy. CrystEngComm, 12, 1590–1599.

Picard, A., Oger, P.M., Daniel, I., Cardon, H., Montagnac, G., and Chervin, J.C. (2006) A sensitive pressure sensor for diamond anvil cell experiments up to 2 GPa: FluoSpheres®. Journal of Applied Physics, 100, 34915.

Pippinger, T., Miletich, R., Merlini, M., Lotti, P., Schouwink, P., Yagi, T., Crichton, W.A., and Hanfland, M. (2015) Puzzling calcite-III dimorphism: crystallography, high-pressure behavior, and pathway of single-crystal transitions. Physics and Chemistry of Minerals, 42, 29–43.

Popkov, Yu.A., Eremenko, V.V., Fomin, V.I., and Mokhir, A.P. (1972) Kombinacionnoe rasseyanie sveta v antiferromagnitnom siderite (Raman light scattering in antiferromagnetic siderite). Fizika Tverdogo Tela (Solid State Pysics), 14, 2294–2299.

Ragan, D.D., Gustavsen, R., and Schiferl, D. (1992) Calibration of the ruby R_1 and R_2 fluorescence shifts as a function of temperature from 0 to 600 K. Journal of Applied Physics, 72, 5539–5544.

Redfern, S.A.T. (2000) Structural variations in carbonates. Reviews in Mineralogy and Geochemistry, 41, 289–308.

Reeder, R.J., and Markgraf, S.A. (1986) High-temperature crystal chemistry of dolomite. American Mineralogist, 7, 795–804.

Rohrbach, A., and Schmidt, M.W. (2011) Redox freezing and melting in the Earth's deep mantle resulting from carbon-iron redox coupling. Nature, 472, 209–212.

Ross, N.L., and Reeder, R.J. (1992) High-pressure structural study of dolomite and ankerite. American Mineralogist, 77, 412–421.

Rutt, H.N., and Nicola, J.H. (1974) Raman spectra of carbonates of calcite structure. Journal of Physics C: Solid State Physics, 7, 4522–4528.

Saloman, E.B., and Sansonetti, C.J. (2004) Wavelengths, energy level classifications, and energy levels for the spectrum of neutral neon. Journal of Physical and Chemical Reference Data, 33, 1113–1158.

Schiferl, D., Nicol, M., Zaug, J.M., Sharma, S.K., Cooney, T.F., Wang, S.-Y., Anthony, T.R., and Fleischer, J.F. (1997) The diamond $^{13}C/^{12}C$ isotope Raman pressure sensor system for high-temperature/pressure diamond-anvil cells with reactive samples. Journal of Applied Physics, 82, 3256–3265.

Spivak, A., Solopova, N., Cerantola, V., Bykova, E., Zakharchenko, E., Dubrovinsky, L., and Litvin, Y. (2014) Raman study of $MgCO_3$-$FeCO_3$ carbonate solid solution at high pressures up to 55 GPa. Physics and Chemistry of Minerals, 41, 633–638.

Tropper, P., and Manning, C.E. (2007) The solubility of corundum in H_2O at high pressure and temperature and its implications for Al mobility in the deep crust and upper mantle. Chemical Geology, 240, 54–60.

Valenzano, L., Noël, Y., Orlando, R., Zicovich-Wilson, C.M., Ferrero, M., and Dovesi, R. (2007) Ab initio vibrational spectra and dielectric properties of carbonates: magnesite, calcite and dolomite. Theoretical Chemistry Accounts, 117, 991–1000.

Wagner, J.M. (2000) On the inadequacy of linear pressure dependence of vibrational frequency. Solid State Communications, 116, 355–356.

Watenphul, A., and Schmidt, C. (2012) Calibration of berlinite ($AlPO_4$) as Raman spectroscopic pressure sensor for diamond-anvil cell experiments at elevated temperatures. Journal of Raman Spectroscopy, 43, 564–570.

Williams, Q., Collerson, B., and Knittle, E. (1992) Vibrational spectra of magnesite ($MgCO_3$) and calcite-III at high pressures. American Mineralogist, 77, 1158–1165.

Xu, J., Kuang, Y., Zhang, B., Liu, Y., Fan, D., Zhou, W., and Xie, H. (2015) High-pressure study of azurite $Cu_3(CO_3)_2(OH)_2$ by synchrotron radiation X-ray diffraction and Raman spectroscopy. Physics and Chemistry of Minerals, 42, 805–816.

Ye, Y., Smyth, J.R., and Boni, P. (2012) Crystal structure and thermal expansion of aragonite-group carbonates by single-crystal X-ray diffraction. American Mineralogist, 97, 707–712.

Zhang, J., and Reeder, R.J. (1999) Comparative compressibilities of calcite-structure carbonates: Deviations from empirical relations. American Mineralogist, 84, 861–870.

Manuscript received December 19, 2017
Manuscript accepted August 31, 2018
Manuscript handled by Mainak Mookherjee

Downloaded from https://pubs.geoscienceworld.org/msa/ammin/article-pdf/103/12/1988/4574485/am-2018-6442.pdf
by University of Arizona user
on 17 December 2018